

Developing a Step by Step Understanding of Physical and Microstructural Features of HVOF Coatings by Impedance Spectroscopy Modelling

Akbar Niaz^{1*}, Muhammad Iftikhar Faraz², Abdulaziz Hassan Elsinawi¹
and Muhammad Atiq Ur Rehman³

¹Materials Engineering Department, College of Engineering, King Faisal University, Saudi Arabia.

²Mechanical Engineering Department Collage of Engineering King Faisal University, Saudi Arabia
Al-Hofuf. P.O.Box.380, Al-Hasa 31982, KSA.

³Department of Materials Science and Engineering, Institute of Space Technology Islamabad,
Islamabad 44000, Pakistan.

Authors' contributions

This work was carried out in collaboration among all authors. All authors read and approved the final manuscript.

Article Information

Editor(s):

(1) Dr. Madogni Vianou Irene, Universite d'Abomey-Calavi (UAC), Benin.

Reviewers:

(1) Marwa Mohamed Nabil Hamouda, Advanced Technology and New Materials Research Institute, Egypt.

(2) Aqel Mashot Jafar, Solar Energy Centre, Iraq.

Complete Peer review History: <http://www.sdiarticle4.com/review-history/69155>

Original Research Article

Received 05 April 2021
Accepted 15 June 2021
Published 18 June 2021

ABSTRACT

The corrosion of HVOF metallic coatings is a complex electrochemical process where numerous physical and electrochemical processes occurred at the surface. Researchers have adopted different approaches to study these processes. A significant cache of research material is available online, where researchers have reported electrochemical corrosion testing techniques complemented with passive layer characterization and microstructure analysis. Some others published their work supported by complicated mathematical modelling concepts and equations. This study focuses on developing a step-by-step understanding of the physical and microstructural features of HVOF coatings by electrochemical impedance spectroscopy. First, the different physical characteristics of the coating are envisaged, and their corresponding equivalent circuit models are constructed. Second, using simulation software, the impedance of each circuit is

simulated by giving seed values to each circuit component. Third, after building up the necessary background, a model is constructed for the HVOF Inconel 625 coatings to see the quality of fit with the experimental data. Although the quality of fit is not perfect, still, the step-by-step modeling and simulation of the corrosion processes at the coatings add value to the knowledge in electrochemical corrosion testing.

Keywords: HVOF coatings; corrosion testing; electrochemical characterization; HVOF coatings feature modeling; impedance spectroscopy; simulation and analysis.

1. INTRODUCTION

The corrosion and wear resistance of the inexpensive metallic materials is increased by using thermal spray coatings. One of the methods for producing such coatings is high-velocity oxygen fuel coating (HVOF). The HVOF coating is a build-up of many semi-molten particles that strike on the workpiece at a very high velocity. While traveling from spray gun to the workpiece, the particles interact with the surrounding air and form oxides. These oxides appear as dark spherical rings in-plane and as a series of dark stringers in cross-section [1]. Additionally, pores and cracks are produced in the coating due to incomplete melting of the particles in layers and interlayers. Moreover, the non-thermodynamic cooling of the coatings also causes variation in compositions from one part of the coating to another. The irregular particle size and hard phases of the wear-resistant coatings produce a surface profile that is highly heterogeneous from place to place.

Different researchers carried out their work on microstructure examination and corrosion performance of the coating by using microstructure evaluation, composition analysis, and electrochemical testing methods [2,3]. The electrochemical methods reported in various research works are open circuit, potentiodynamic polarization, galvanic corrosion and electrochemical impedance spectroscopy (EIS) [4-6]. Most of the reported data only covered the applied part, aside from a few published in-depth studies of a particular aspect of coatings. As the focus of this article is on EIS modelling of the HVOF coatings, research work relevant to the impedance spectroscopy of the coatings has been presented here.

Ahmed et al. reports the existence of a compressed semi-circle in WC-Co coatings. They attributed these semi-circles to a limited diffusion reaction and a non-continuous oxide layer. They also correlate two-time constant behavior to WC-phase and the matrix phase. This correlation seems logical, as

electrochemical nature of WC-phase is much different from that of the Co-binder phase; the Co-binder phase is anodic to WC-phase. The difference of electrochemical nature also supports the formation of a non-continuous oxide layer as WC-phase does oxidize with the Co-phase. The interpretation of the equivalent circuit model and the model fitting with experimental data also add further value to the EIS study. In their research, they also suggested the need for further refining in the EIS modelling for a better understanding of corrosion processes taking place at HVOF coatings [7].

Additionally, Sadeghimersht et al. used impedance spectroscopy as a corrosion investigation tool in their work on Fe and Co-based HVOF coatings. The equivalent circuit model for curve fitting consists of a CPE, a capacitor, a charge transfer resistor, and a solution resistor. A non-adherent porous corrosion product alongside capacitance double layers were taken as the primary impedance contributing parameters. The rise in charge transfer resistance and the rise in capacitance are the parameters attributed to higher corrosion performance [8].

Hong et al. reported the effect of spray parameters on the corrosion performance of WC-Co-Cr coatings. They reported the small diameter semi-circle of the Nyquist plot as the lower corrosion-resistant material and the larger diameter of the semi-circle of the Nyquist plot as the higher corrosion-resistant material. The main components of the equivalent circuit model were pore resistance, coating resistance, solution resistance and capacitance related to pores and the coating layer. Furthermore, they reported enhanced impedance as the improved corrosion resistance of the material [9].

Melero, Sakai, et al. carried out their corrosion resistance evaluation work on HVOF TiO₂-hydroxyapatite coatings. They reported the higher corrosion resistance for the mixture 80% hydroxyapatite and 20% TiO₂ sample. Additionally, they attributed the higher capacitive

loop of the Nyquist plot to higher corrosion resistance. They found two-time constants in the impedance spectra; one they related to the dielectric properties of the coatings while the second they associated with the interfacial process (corrosion process). They have not reported the relevant circuit model or impedance quantities [10].

Verdian et al. studied NiTi coatings on mild steel deposited by the HVOF method. In their EIS results, they merged coating capacitance with the dielectric process of the surface and coating resistance with the pore resistance [2]. They used an equivalent circuit model that is like Randal's model. The EIS work was carried out for 14 days, and it reported higher impedance at the start and end. The higher impedance at the beginning attributes to the overall resistance of the coating, while a gradual increase in the impedance relates to the pore sealing and oxide formation. These processes enhance the impedance values.

Suegama et al. reported their corrosion study on HVOF Cr₃C₂-NiCr coatings by changing the gun transverse speed. The equivalent circuit model contains two-time constants; one corresponds to pores and second to the coatings. Due to the roughness of the coatings, they have used a constant phase element instead of the capacitive element. In their results, they reported high impedance values for the coatings carried out at a high transverse speed. Additionally, they attributed the higher impedance values to low porosity and less flight oxidation of the powder particles during the HVOF process [11].

Guilemany et al. studied the role of coating thickness for corrosion properties of the coatings. They revealed that HVOF coatings work as barrier coatings. Thin coatings do not stop the penetration of the electrolyte to the substrate, while thick coatings develop stresses and cracks, which cause infiltration of the electrolyte to the substrate. The CPE was used due to the rough surfaces of the coat. Furthermore, a two-time constants circuit was used to represent impedance due to pores and second with dielectric impedance. The higher impedance and capacitance values were attributed to the high corrosion performance of the coatings [12].

Electrochemical impedance spectroscopy supported with scanning electron microscopy and energy dispersive X-ray spectrometry (EDS) analysis was used by Ali et al. to characterize the corrosion properties of the thermal barrier

coating bond coat. The NiCrAlY bond coat was deposited on Haynes-230 alloy, and the samples were heated from 700 to 1200°C for different intervals of time. The structural composition and compound formation analysis was carried out before and after thermal cycling [13]. The change in electrical properties, resistance, and capacitance, were related to the microstructure and microchemistry of the thermally grown oxide (TGO). In the early stage of thermal cycling, the impedance increased due to the formation of thermally grown Al₂O₃ and reached to the maximum value after 100 hours. With further thermal cycling, the TGO changed from Al₂O₃ to a mixture of Cr₂O₃, (Ni, Co) (Cr, Al)₂O₄ spinel oxide. The spinel oxide is porous, and although thermal cycling increased the thickness of oxide, the impedance decreased [13].

Antou et al. tries to quantify the interconnected porosity by comparing the polarization resistance of the coated and uncoated samples. They assume that the surface passivates after some time, and resistance only related to the interconnected porosity. The simple Randal model is used to quantify the impedance parameters of the uncoated sample, while a commonly used model for porosity is used for the coated surface. Two times constant were observed for the coated samples, which were related to the coating electrolyte and pore electrolyte processes. It is also reported that coating does not show the capacitive behavior hence used a CPE component instead of a capacitor [14].

Amsellem et al. worked on 3-D simulation of porosity of plasma spraying coatings. They reported in their study impedance increases due to an increase in open porosity while decreases due to interconnected porosity. Although they were not able to completely define the pore geometry with the EIS study yet, they were able to prove that coating resistance is related to the % porosity in the coatings. In their work, they also reported that open porosity is responsible for increasing resistance to any laser surface treatment [15].

The EIS work carried out by Bolleli for microstructure and tribological investigation revealed that there is a linear relationship between the coating resistivity and porosity. Within this study, they also compared interconnected porosity of High-velocity suspension flame sprayed (HVSFS) coatings with atmospheric plasma spray coatings (APS), and

high-velocity oxygen fuel coatings (HVOF). The quantification of the EIS parameters was carried out by equivalent circuit models [16], which revealed that coatings produced by the HVSFS process provide the least porosity as compared to the rest of the methods [17].

Thermal barrier coatings are extensively used to study corrosion processes taking place at interfaces. Chen et al. carry out such studies; they reported two semi-circles for the Ytria-stabilized-zirconia; the one at higher frequencies is attributed to the top-ceramic coat while the second related to the thermally grown oxide. The semi-circles of the Nyquist plot were depressed ones, which is the peculiar nature of the impure capacitor called capacitance phase element. The impedance of the TGO increases with the temperature due to an increase in the thickness [18].

Cheng et al study effect of crystallization on the corrosion resistance in arc sprayed Fe-based coatings. The amorphous coatings were heat-treated to different levels to partial crystallization. These coatings were later compared with as-received coatings to see the change in their impedance response. The height of the CPE and impedance value of the heat-treated sample decreases as a function of an increase in the crystallization. The decrease in impedance as a function of crystallinity indicates that the transfer from amorphous to crystallinity negatively affects the corrosion performance of the coatings [19].

Cojcoaru et al. studied the resistive and dielectric properties of the Mg-rich coatings. In their study, they reported the porosity as a primary contributor for changing the resistive and dielectric properties. The pores filled with air causes a decrease in coating capacitance, which causes the lowering of the dielectric constant [20].

Chenchen et al. also studies oxidation and corrosion processes of nanostructured thermal spray coatings. They reported impedance spectroscopy as a tool to reveal microstructural changes during different intervals of sintering time. The impedance spectra of all coating showed three relaxation processes. The processes were related to YSZ- grains, YSZ-grain boundaries, and electrode response. The change in microstructure features was fast for 10 hours of sintering time as compared to more extended time. The higher capacitance at the initial stage, they correlated to the no of pores, where each pore contributes to the total

capacitance of the coatings. An increase in sintering time causes pore sealing and hence decreases in the coating capacitance. The rise in the grain resistance is attributed to the increase in grain size which increases at the cost of losing nano-structure of the YSZ for the 10 hours of sintering time [21].

It can be seen from the above literature survey that researchers have extensively used EIS as a tool for measuring corrosion performance, but generally, the results are presented as a supportive link between the other techniques. Although the impedance spectrum itself is beneficial, the presented results with the equivalent circuit model enhance their values. In some of the above-reported research work, the equivalent circuit model (ECM) is entirely missing. Some of the papers establish linkage between equivalent circuit models and impedance spectra, but a logical expression of the circuit component configuration is not expressed. In this study, a systematic approach is adopted to elucidate each circuit component and link with coating physical feature. The impedance spectra are linked with the physical feature, and changes in the impedance spectra with a change in physical features are simulated by using a free non-commercial software, "EIS spectrum Analyzer" [22]. The presence of a physical feature and its circuit is configured to demonstrate the impedance changes. The components of the subsystems were merged to see the difference in the simulation graphs. The data is extracted from the software in text files and re-plotted in excel sheet to re-generated the data [22]. After embedding all physical features, the most reported model and the proposed models are fitted with the impedance spectra of the Inconel 625 coatings. It was found that although the quantification of the impedance parameters is not remarkably improved, but curve fitting is improved between experimental data and simulated data. Hence, this modeling and simulation exercise contributes towards better understanding of corrosion processes taking place at the HVOF coating surfaces.

2. EXPERIMENTAL METHODS

The coating for impedance spectroscopy tests was prepared by using the gas atomized Inconel 625 powder with the size range from 20 μm to 50 μm , purchased from William Rowland Limited (Sheffield, UK). The coatings were produced by using Met-Jet III equipment of Metallization Limited (Dudley, UK). Mild steel coupons with

dimension of $3 \times 40 \times 60$ mm were used as substrate material. These coupons were grit blasted before coatings to enhance bonding. The powder used for coating and process parameters for producing coatings are given in the Table 1. Multilayer passes of the powder stream produce a coating thickness of 300 μm .

The epoxy embedded 10 mm^2 coating samples were progressively grinded and polished to achieve a surface finish of $< 1 \mu\text{m}$. The average surface roughness of the coatings was 0.68 on 5 mm^2 by using Talysurf CLI 1000-3D system from Taylor Hobson Limited (UK).

The corrosion tests were carried out in 0.5 M H_2SO_4 solution by using ACM potentiostat (UK). The coating samples were submerged in electrolyte for one hour for stabilization before recording impedance spectra over a frequency range from 10^{-1} Hz to 5×10^3 Hz. The impedance data was fitted with the already existed model and proposed model to check the quality of fit.

3. RESULTS AND DISCUSSION

3.1 Modeling and Simulation of Coating Physical Features

The microstructure of most of the engineering materials, especially of HVOF coatings, is heterogeneous, i.e., having pores, cracks, grain boundaries, inclusions, phases of different electrochemical activity, oxides. Furthermore, keeping material in a specific electrolytic environment for a long time and changing the physical parameters, e.g., temperature or applied potential, can all significantly affect the electrochemical properties and hence, EIS responses of materials. The first physical features of the HVOF coating are considered as subsystems; subsequently, their presence in the coating is configured in the electrical circuit to simulate impedance response. The impedance response is modelled to understand the changes in spectra due to the change in circuit components and their quantities. The physical features considered are surface roughness, porosity, layered oxides, dispersed oxides, and a combination of them. Table 2 presents the schematic, circuit configuration and physical explanation in shorthand.

3.1.1 Surface roughness

Smooth looking surfaces can be significantly different at the micro-level, and the case is even worse for coated and sintered objects. Due to this fact, the electrode-electrolyte interface is not

at equipotential; even for purely resistive interface impedance, it is independent of local current density [4,23]. The higher the current density at a point, the higher the potential drop across the interface, which, in turn, tends to lower the local current density. Therefore, the tendency is to make a uniform current distribution, called the smoothing effect. The magnitude of the smoothing depends on the interface and bulk impedance, as well as the geometry of the system.

3.1.1.1 Equivalent circuit model to represent roughness

Fig. 1 presents the modified version of the Randal model used to simulate the surface roughness. The capacitor element (Cdl) of the circuit is replaced with a constant phase element (CPE). The CPE represents the impure capacitance at the rough surface with parameter P and exponent n . For the ideal capacitor, the exponent factor for CPE is generally considered as 0.9–1, while it is 0.6–0.9 for non-ideal capacitors [24]. The exponent of the CPE can be related to the surface roughness of the electrode. The higher the surface roughness is, the lower the exponent of CPE will be. R_u and R_p are the solution and polarization resistance across the substrate electrolyte interface, respectively, as shown in Fig. 1. In our experimental work, all in the later stage samples were polished to $\leq 1 \mu\text{m}$ surface finish; hence, this is not expected to be a significant effect in the results [4,23].

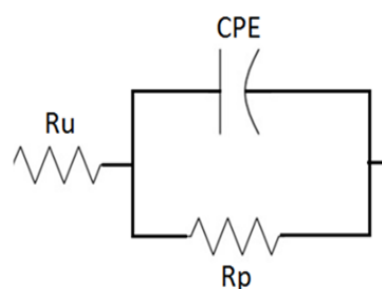


Fig. 1. Modified Randal model for rough surface

3.1.1.2 EIS simulations for surface roughness

Fig. 2a, 2b, and 2c show simulated EIS graphs from an ideal to a real surface. In the given model, R_u is the uncompensated solution resistance between working and reference electrode; CPE is a constant phase element at metal electrolyte interface, while R_p is polarisation resistance/charge transfer resistance across the double layer. In Fig. 2a of the Nyquist

plots, the hollow squares graph represents that the electrode surface is perfectly smooth and the constant phase element (CPE)= C, i.e., $Y_0 = 1/Z_{CPE} (j\omega)^n$, where exponent n is 1. In real systems, electrode surfaces are rough and inhomogeneous, which does not give a pure capacitive response. This impure capacitive response is presented by taking the CPE exponent values 1 to 0.80. The changes can be seen from the Nyquist plots in Fig. 2a, the Bode impedance plots in Fig. 2b and Bode theta plot in Fig. 2c. The Nyquist plots in Fig. 2a show the semi-circle being gradually depressed with a decrease in the “n” value. There is an imaginary impedance change from 50 $\Omega \text{ cm}^2$ to 30 $\Omega \text{ cm}^2$. The change in the impedance can be correlated to change from a capacitive behavior to resistive behavior of the coatings. The fact is further clear from the Bode impedance graph Fig. 2b, where the slope of the graphs increases with a decrease in the “n” value. The characteristic property of the capacitor is that its impedance varies with change in frequency. The faster change is near to the ideal capacitor than the one with a slower transition. The bode impedance plots in Fig. 2b show approximately vertical in the impedance changing region, while the slope of the line decreases with decreasing “n” value. The plateau at high frequencies and low frequencies belong to solution resistance and polarization resistance. All parameters of the circuit were kept constant to see only changes due to the exponent “n” values. The Bode theta plot in Fig. 2c also shows that the magnitude of the peak alongside its position shifts from low frequencies to high frequencies with a change in “n” value from 1 to 0.8. Hence, it can be established from these simulations that change in the spectra shape, impedance quantities, and their peak position significantly affect the surface roughness factor. The shift in spectra shape will be even more if the P factor of the constant factor changes.

3.1.2 Porosity effect

Porosity also significantly contributes to the overall impedance of the system, especially in coatings. Pore numbers, the situation within the pore, and interconnected or segregated pores can add considerably to the degradation process [3,25]. The overall percentage of porosity reported in HVOF coatings is from 3–8%, while for the sintered structures, the percent porosity is reported to be even higher than HVOF coatings.

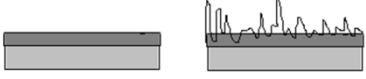
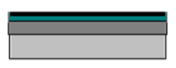
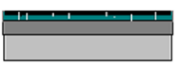
3.1.2.1 The equivalent circuit for porous coating

Fig. 3 presents the equivalent circuit model and schematic diagram for the porous HVOF coatings. In the equivalent circuit, R_u is an uncompensated solution resistance between the reference and working electrodes. The solution resistance of an ionic solution depends on the nature of ions, their concentration, and temperature of the solution, and electrodes' geometry. R_{pore} is the resistance offered to mass transport toward and away from the pore due to the geometry effect and processes taking place with the pore. CPE_{coat} is the coating capacitance between the electrolyte and coating interface due to charge accumulation. Cdl is the capacitance double layer at the substrate metal interface when the electrolyte seeps through the pores and interacts with the substrate. R_p is polarization resistance/charge transfer resistance across the substrate electrolyte interface. R_u is in series with the combination of coating capacitance and pore resistance. Additionally, it is in series, as the current flow path does not change while R_{pore} is in parallel with CPE_{coat} due to charge transfer reaction across the capacitive layer. Macro pores allow the electrolyte to pass through and interact with the substrate to form Cdl and polarization, offering an alternative current path; hence, this combination is in series with the pore resistance.

Table 1. Inconel 625 powder composition and HVOF coating process parameters

Inconel 625 powder							
Element	Ni	Cr	Mo	Nb			
Weight %	65	22	9	4			
Coating process parameters							
Sample	O ₂ flow rate (L/min)	Fuel flow rate (L/min)	N ₂ flow rate (L/min)	Nozzle length (mm)	Spray distance (mm)	Powder feed rate (g/min)	Number of passes
Inconel 625	910	0.48	4.6	100	350	78.7	24

Table 2. A summary of subsystems and their ECM circuitry in HVOF metallic coating

Subsystems	Schematic	Circuits configurations	Physical explanation
Surface roughness		$R_u - \text{RC}_{coat}$	Pure capacitive to impure capacitive
Porosity		$R_u - \text{RC}_{coat} - \text{RC}_{pores}$	Resistance decreases with increase in % porosity
Layered oxides		$R_u - \text{RC}_{oxide1} - \text{RC}_{oxide2}$	Layered oxides provide one path for charge flow
Dispersed oxides		$R_u - \text{RC}_{oxide1} - \text{RC}_{oxide2}$	Dispersed oxides provide a separate path for charge flow
Layered oxides + porosity		$R_u - \text{RC}_{oxide1} - \text{RC}_{oxide2} - \text{RC}_{pores}$	Layered oxide provides the same path while pores provide a separate path for charge flow
Dispersed oxide + porosity		$R_u - \text{RC}_{oxide1} - \text{RC}_{oxide2} - \text{RC}_{pores}$	Each oxide and pores provide a separate path for charge flow
Layered oxides + dispersed oxides + porosity		$R_u - \text{RC}_{oxide1,2} - \text{RC}_{oxide, pores}$	Layered oxides and pores + dispersed oxide provide a separate cumulative path

$R_u =$ Solution resistance; $RC =$ Time constant (resistance and capacitance of the component)

3.1.2.2 EIS simulations for porosity

The equivalent circuit model results in Fig. 4a, 4b, and 4c display the changes in the impedance spectra when pore resistance is changed. It was assumed that half of the impedance is due to the coating ($R_p Cdl_{coat}$), while half is due to pores ($R_{pore} CPE_{pore}$). The circuit components quantities were considered constant except those contribute considerably. The seed values of R_{pore} were used as 10 Ω , 50 Ω , 100 Ω , 200 Ω and 1000 Ω to simulate the R_{pore} as 1%, 5%, 10%, 20%, and 50%. It can be seen from the Nyquist

plots in Fig. 4a that the size of the semicircle increases with a decrease in porosity. The impedance is directly related to the number of pores and their resistance in the coatings. Furthermore, the Nyquist plots do not show separate time constants for coatings and pores, and instead, they show the resultant impedance of the circuit.

In Fig. 4b, the higher frequencies side plateau is the same for all five simulations as solution resistance is the same for all. The lower frequencies side of the plateau shows a gradual

rise with the decrease in porosity. This plateau is the resultant impedance of the resistors involved in slow corrosion processes, i.e., R_{pore} and R_p . The highest value of impedance can be seen for the lowest porosity. The slope of the graphs from 1–10 Hz shows the same negative impedance slope, indicating that the property of the capacitor is not changing.

Furthermore, this fact is clear from the perfect semicircles of the Nyquist plots. The Bode theta plots Fig. 4c shows a shift of the angle peaks

toward higher frequencies alongside dividing one peak to be defined as two peaks for 5% and 10% porosities. It can be concluded that that extremely low and extremely high porosity does not change the shape of the impedance spectra but cause a change in resultant impedance values. It partially appears as a small-time constant in the Nyquist plot and increases in the low-frequency plateau. The difference due to porosity can also be observed in the Bode theta plot, where a slight bend is seen on the high frequencies data.

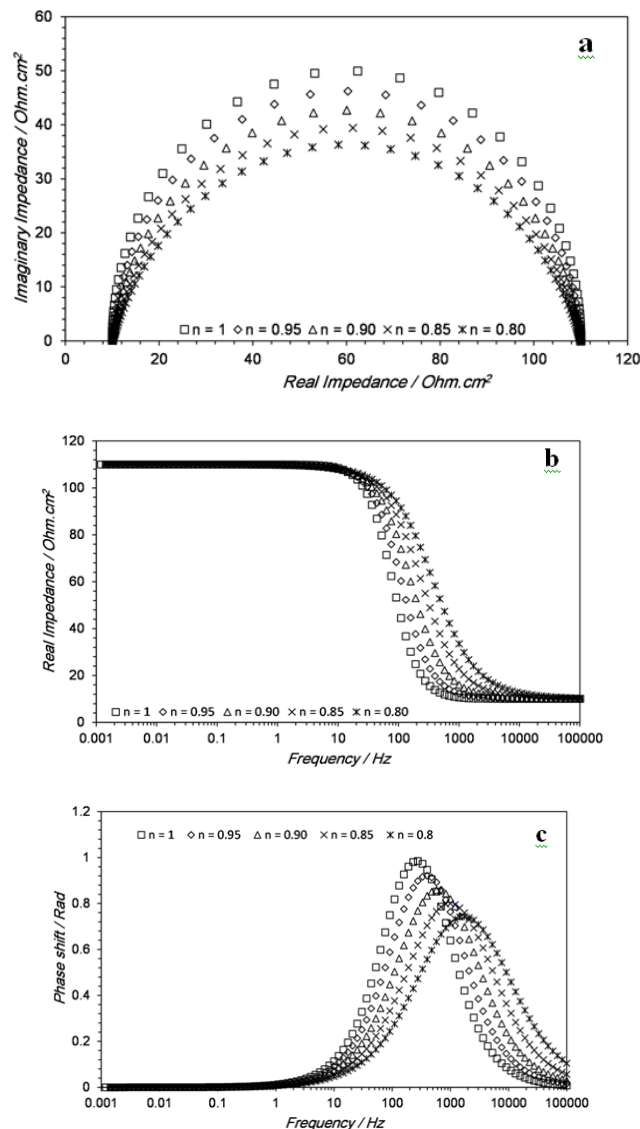


Fig. 2. EIS graphs, a) Nyquist plots, b) Bode impedance plots, c) Bode theta plots. In each set of plots the capacitance values of CPE element is varied by changing the exponent values 1 to 0.8 (i.e. $CPE = P \times n$, P is capacitance and n is exponent). The exponent value decreasing from 1 indicates deviation from pure capacitor behavior. The solution resistance and polarization resistances were kept constant as 10 Ω and 100 Ω respectively

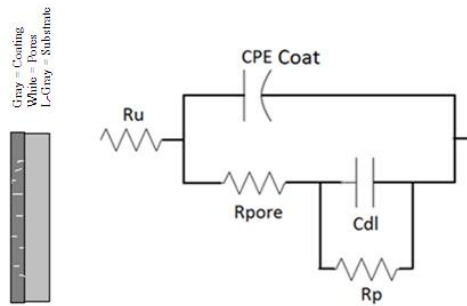


Fig. 3. Equivalent circuit model of the porous coating [26]

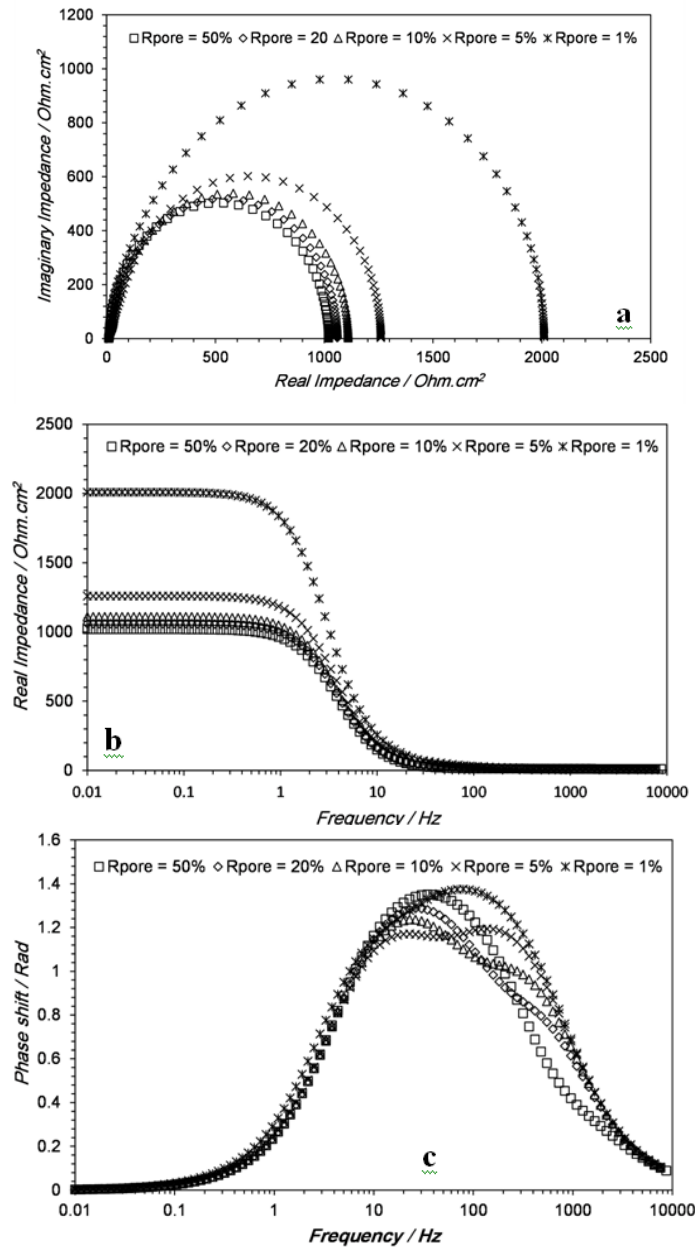


Fig. 4. EIS graphs; a) Nyquist plots, b) Bode impedance plots, c) Bode theta plots simulation by using the equivalent circuit model in Fig. 2 with the fixed quantities of $R_u = 10 \Omega$, $R_p = 1000 \Omega$, $P = 20 \mu F$, $n = 1$ and variable R_{pore} from 1 to 0.8 to simulate different levels of roughness

3.1.3 Microstructure features

It is rare to use pure metals in engineering applications; even with the pure metals, there are grain boundaries (regions of disorder) that have different electrochemical activity as compared to the core of the grain. Alloys may have multiple phases present; the two times constant model can be used for two phases of different electrochemical activity, various oxides, oxide growth, and grain boundary effects [27].

In polycrystalline solids, electrolytic transport properties are strongly affected by microstructure, and the impedance spectra usually contain features that can be related to microstructure [4,23,28,29]. The early microstructural studies by EIS were carried out on ceramics due to different conductivities of the phases, e.g., zirconia and β alumina. Different impedances at grain core, boundaries, grain boundaries accumulations, different phases, and less/more protective oxides can be displayed as different time constants if their RC values are sufficiently different. The hypothetical models describe these microstructures, i.e., parallel or series layer, bricklayer, the Debye grain boundary accumulation model [30].

3.1.3.1 An equivalent circuit for microstructure features

The equivalent circuit models given in Fig. 5 and Fig. 6 represent the different microstructural features in series (layers) and parallel (dispersed), respectively. These models are applicable for oxides but can be used for materials having phases of different electrochemical activity. Theoretically, the EIS results can be used as a complementary technique with SEM to define the partial fraction of each microstructure.

The schematic diagram in Fig. 5 shows two dense and defect-free oxide layers (black and blue) on the coating. The schematic model is configured to elucidate the multi-components coating system in a corrosive environment where different oxides can form. The coating and its bond with the substrate are defect-free; hence, both act like one conductor. No reaction at the substrate/coating and coating/oxide interface is modelled in the circuit, as there is no interaction between the electrolyte and the interfaces (substrate and coating). The solution resistance is in series with the capacitance and resistance combination of both oxides. The current passing

through both oxides is in series, and hence, the equivalent circuit is arranged in series. Within each oxide layer, there is capacitance, which is in parallel with polarization resistance. The opposite extreme is considered in the Fig. 6 schematic, where both oxides are parallel with each other, as they provide different paths for current flow. In real oxidation, neither extreme exists, as oxides do not fully grow in a layer or on localized regions of the structure. The series/parallel decision is made according to the predominant factor in the system, e.g., the oxide growth at the metal surface is predominantly a layered structure while the oxides embedded in the coating is dispersed.

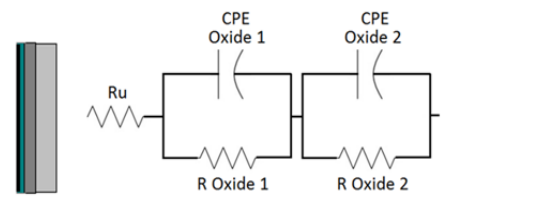


Figure 5: Equivalent circuit model for different oxides in the series

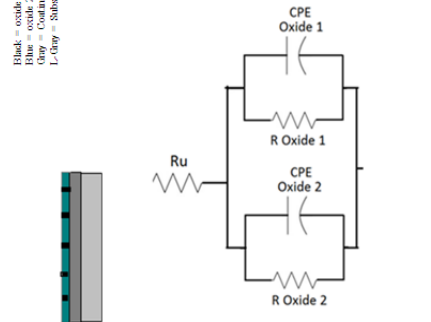


Fig. 6. Equivalent circuit model for different oxides in parallel

3.1.3.2 EIS simulations for microstructure features

The EIS graphs in Fig. 7a, 7b, and 7c are simulated by using the equivalent model in Fig. 5. The impedance spectra were projected by assuming quantities of each of the circuit components. These quantities are related to the physical features of the coatings. The change in some of these quantities is linked to the change in the physical features.

Furthermore, Fig. 7a, 7b, and 7c show a set of three Nyquist, Bode impedance, and Bode theta plot, where all of the values of the circuit components were kept constant except the R_{oxide1} , the amount of which is changed from 10Ω , 100Ω to 1000Ω . The RC_1 is the time constant for the first oxide, while RC_2 is the time

constant for the second oxide. The resistance increase is related to the thickening of one of the oxides of the coating. The height of the semi-circle in the Nyquist plot in Fig. 7a increases with the gradual increases in R_{oxide1} . Having two time constants in the equivalent circuit, it was expected to see two distinct semi-circles in the spectra. The appearance of distinct semi-circles is obstructed probably due the chosen seed values. The Nyquist plots shows data accumulation around the origin of the graph. This is probably the second semi-circle, the effect is visible in bode theta graphs. The seed values of the circuit were chosen to correlate the fact the oxide thickening is very slow and there is not much variation of the oxide layer (approximate similar oxides). It can be established from the shape of the impedance spectra that the formation of a thin and thick oxide layer only changes the overall impedance in the Nyquist plot while the oxide of moderated thickness also changes the shape of the spectra.

Additionally, the cumulative impedance of oxides can also be seen from the Bode impedance graph in Fig. 7b. The impedance plateau at higher frequencies is related to the solution resistance, the negative slope area of the curves is associated with the cumulative impedance of the capacitances (CPE), and impedance plateau at low frequencies is related to cumulative polarization resistance or charge transfer resistances across oxide layers. The Bode theta plot in Fig. 7c shows the highest angle change value when RC_1 and RC_2 are equal, while for the other two graphs, small humps appear, which were obstructed in the Nyquist and Bode theta plots. It is worth noting that the minimal (<10 times) and extremely high (>100 times) relative resistances of the oxides only make a slight difference to the impedance spectra. It is only possible to see these feature if they have relative resistances between the above ranges.

In Fig. 8a, 8b, and 8c, the capacitance of the circuit are taken as 20 μ F, 40 μ F, and 80 μ F to see the change appear in the impedance spectra. The increase in capacitance is to simulate the second oxide to be more stable, compact, uniform, and homogeneous as compared to the first one. The seed values used in impedance spectra were constant except for the capacitor (CPE) component for the oxide₁. The value of the oxide₁ is changed from 20- μ F to 80- μ F.

The change in the EIS graphs is only noticed in the bode impedance and bode theta plots. The

Nyquist plots in Fig. 8a showed the same height of the semi-circle with slight shift in position of the individual data points. The Bode impedance plots in Fig. 8b and the Bode theta plots in Fig. 8c showed change that is more pronounced where capacitive impedance involved. The region of the change is appeared between frequencies, ranges from 10 Hz to 1000 Hz. The increase in the capacitance value from 20- μ F to 80- μ F shift the impedance slope towards lower frequencies. It can be stated that the formation of the oxide with higher capacitance (compact layer-oxide) shift the capacitive impedance to low impedance side. This makes sense as lower frequency side of the bode impedance plot is for slow reactions. The low frequency end in Fig. 8b show the same plateau for all three plots. The lower frequency side of the Bode impedance plot is for polarization resistance, from the graphs appearance we can state, the change in the oxide growth in parallel circuit (layered oxides) does not affect the lower frequency impedance. The effect is same at very high frequency end, which represent the solution resistance. We can conclude from the above results that oxide thickness and compactness does not make much difference in the impedance spectra, the only differences involve at the moderate frequencies.

3.1.4 Porous multiphase microstructure

The above-discussed simplified models do not fully cover the coating system. A coating consists of pores, and, at the same time, the microstructure has regions of different electrochemical activity. The possible combinations of porosity and oxides have been modelled in this section.

3.1.4.1 An equivalent circuit for porous multi-oxide/phases

The model presented in Fig. 9 and Fig. 10 is made by combining the above two features of porosity and different oxides. The oxides in the model are dispersed in the coating microstructure; the dispersed phase provides separate paths for current to flow, which are thus parallel. Pores in the coatings are shallow and distributed throughout the coating and oxides (schematic in Fig. 9). They do not allow the electrolyte to pass through to establish C_{dl} at the substrate; hence, the capacitance at the coating electrolyte (C_{coat}) dominates. Additionally, the given equivalent circuit can be used for dispersed phases of different electrochemical activity, but as stated before; their appearance in the impedance spectra will only be possible

when their time constants are sufficiently different from each other. The oxides having a porous layered structure can be modelled with

two-time constants in series with the parallel coating capacitance and pore resistance.

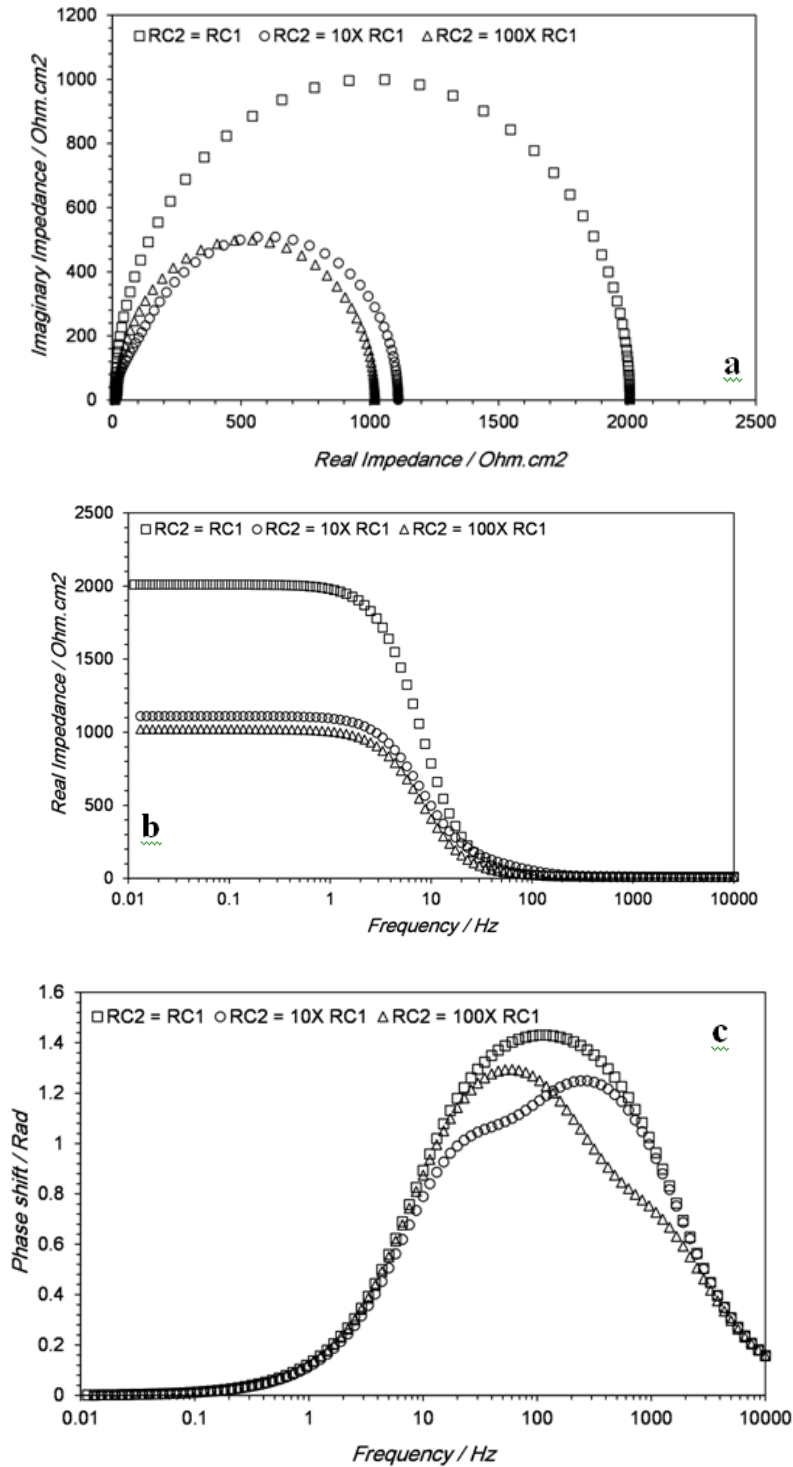


Fig. 7. EIS graphs, a) Nyquist plots, b) Bode impedance plots, c) Bode theta plots simulation by using equivalent circuit model in Fig. 5 with the fixed quantities of all circuit components except the R_{oxide1} , the amount of which is changed from 1000 Ω , 100 Ω to 10 Ω to simulate oxide growth

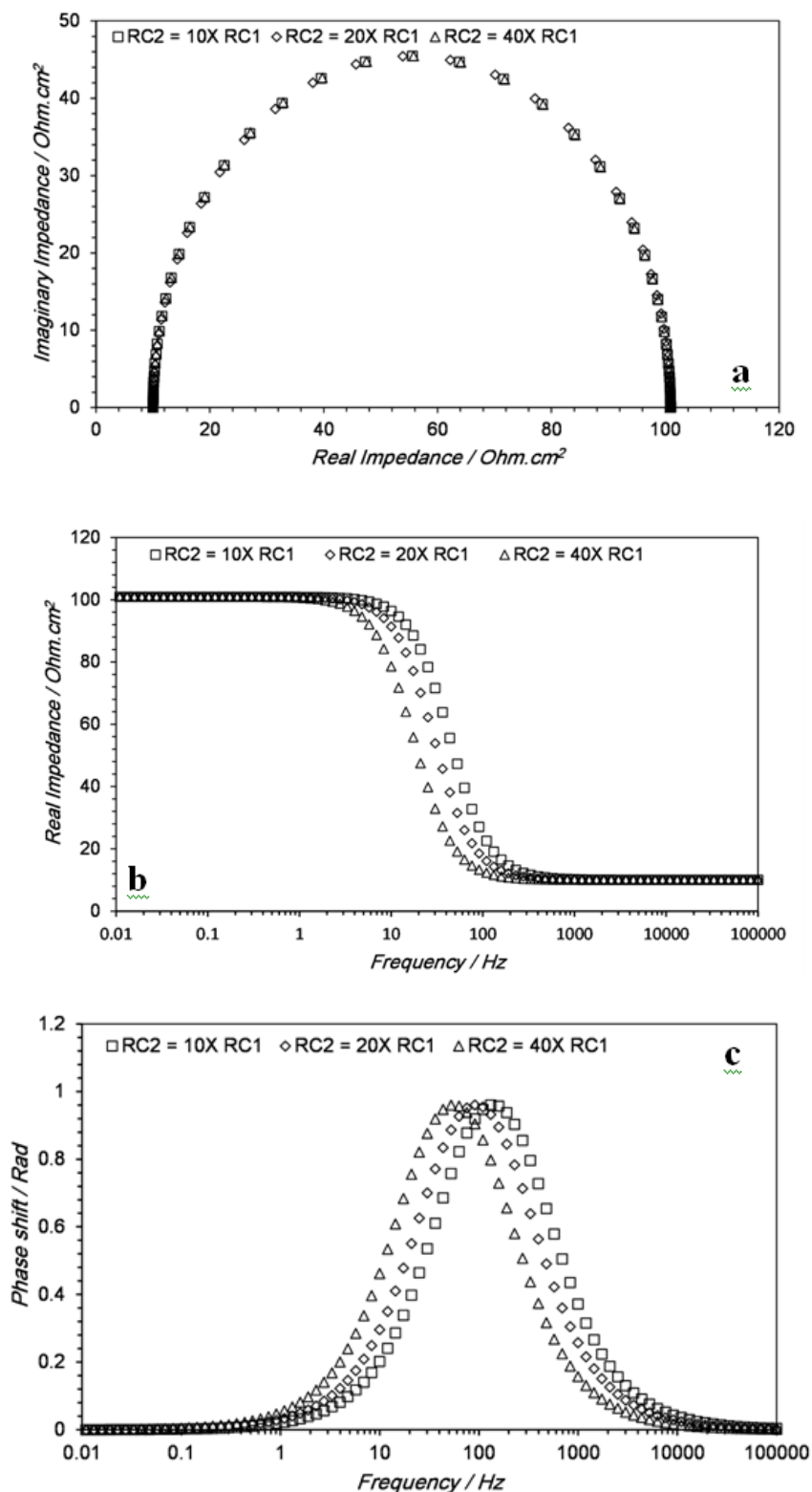


Fig. 8. EIS graphs, a) Nyquist plots, b) Bode impedance plots, c) Bode theta plots simulation by using equivalent circuit model in Fig. 6 with the fixed quantities of all circuit components CPE_{oxide2}, the amount of which is changed from 20 μF, 40 μF to 80 μF to simulate oxide growth with capacitance rise

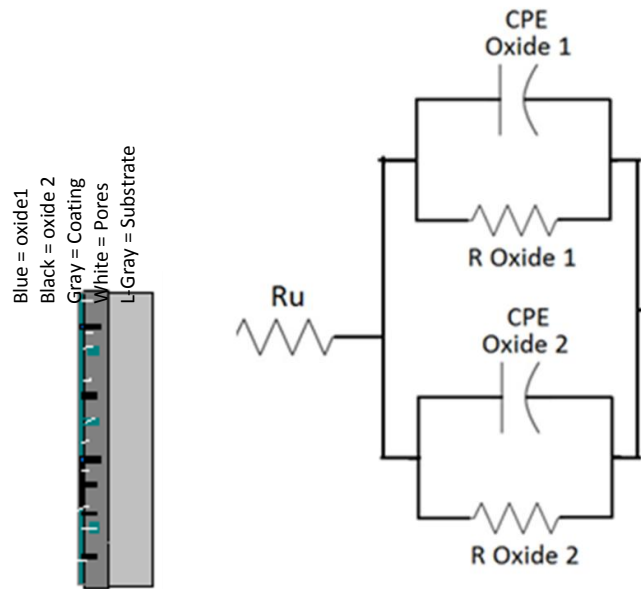


Fig. 9. Equivalent circuit model for pores and oxides (dispersed)

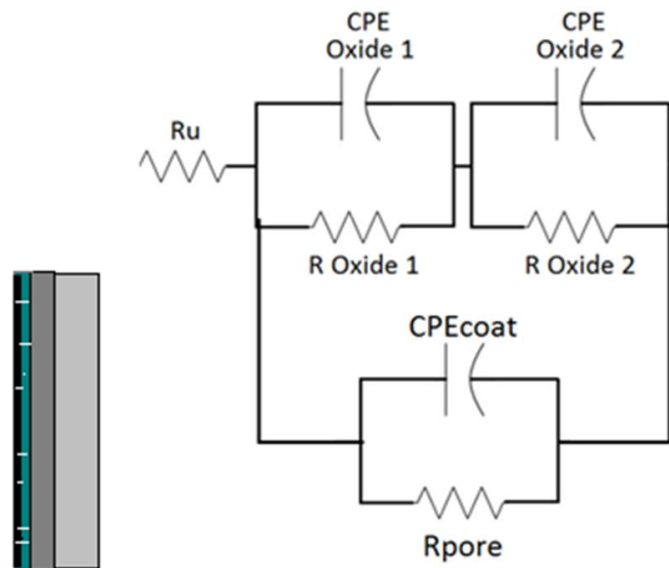


Fig. 10. Equivalent circuit model for pores and different oxides (layered)

The model in Fig. 10 simulates the situation when there are two layers of oxides, and the pores are spread in both layers. It is assumed that oxide growth in the pores only partially blocks the pores, which thus stays in parallel with the oxides. The layered oxides are modelled in series, while the pores are in parallel with both oxides. The model in Fig. 9 shows the combined oxides and then put together with pores in parallel to represent the situation when some pores completely penetrate the coating thickness. The combined effect of the oxides is

considered because of their series combination to show a resultant effect in the impedance spectra.

3.1.4.2 EIS simulation for porous multiphase microstructure

In Fig. 11a, 11b, and 11c, more complex systems are simulated to see the combined effect. The system was considered to have porosity as well as two different phases/oxides. The simulated graphs show the combine Nyquist, Bode

impedance and Bode theta plots for the circuits when oxides are placed parallel and in series. It can be seen from the Nyquist plots in Fig. 11a—a bigger semi-circle when oxides are put parallel in the circuit while an approximately ten times smaller semi-circle when the oxide is placed in the series configuration. Furthermore, it is observed from the circuit that the small feature of the circuit components is obstructed in the impedance spectra and that only cumulative impedance appears. The low frequencies at the end of the impedance values slightly show off the presence of the second oxide.

The same trend can be seen in the Bode impedance graphs in Fig. 11b, where two significant plateaus can be seen. The one at higher frequencies is related to solution resistance, pore, and crack resistance, and the second one is related to charge transfer/polarization resistance of the highly resistive oxide. The gradual increase in the impedance from 100 Hz to 100 Hz is related to the CPE component of the circuits. The second plateau in the Bode impedance also shows a slight slope before reaching a pure resistive mode. The highest impedance value is noted around $10 \Omega\text{cm}^2$ for the oxides in series and $110 \Omega\text{cm}^2$ for the oxides in parallel.

The Bode theta plots in Fig. 11c shows the same trends where the maxing phase change is noted around 1.4 radians for parallel oxide configuration and around 1 radian for the oxides in series. No separate features of the oxides of phases were noticed in the Bode theta plots. Some features may appear in the impedance spectra with changes in the values of circuit components. Furthermore, many variables in the circuit may confuse the situation; to avoid this complication, only changes due to circuit configurations have been considered.

3.1.4.3 EIS simulation for porous multiphase microstructure (dispersed)

The Fig. 12a, 12b and 12c shows the impedance response of the dispersed oxides and pores as presented in the model given in Fig. 9. The coating features are same as of last section, only their orientation in the coatings is changed from layers to disperse. As there is no stringent control of microstructure features during high velocity coating process, it is quite possible to have oxides with the coatings pretty much anywhere (dispersed). The disperse microstructure features can be modeled to a

predominant series circuitry rather as cumulative effect is more apparent in impedance spectra than individuals features.

The Nyquist plots show two semi circles, the clarity increases with increase in the capacitance value. The use of the same values for the parallel circuitry does not showed this clarity, thus it can be established here alongside nature of the microstructure features, their orientations in the coatings also matters to give a specific appearance. The bode impedance and bode theta plot show these characteristics appearances with a frequency range of 1 Hz to 0.1 Hz.

3.2 Linking Hypothetical Models to Real Coatings

After considering each physical feature of the HVOF coatings as shown in Fig. 13a, their equivalent circuit models were made, quantities were assigned to each of the circuit components to simulate impedance spectra, and the amounts of the components were varied to observe significant changes. It is worthwhile to make a model for real coatings and see its quality of fit to the experimental data. A model to include all of the coating features is given in Fig. 13b. The Inconel 625 coating produced by HVOF methods with previously optimized parameters [31] is used to test the equivalent circuit model. The depositing multilayer passes of the HVOF gun produce a coating thickness of 300 μm to 350 μm . The surface of the coating is polished to below 1 μm surface finish. The impedance spectra are recorded in 0.5 M sulfuric acid solution at 25°C in stagnant conditions.

Based on the coating microstructural features and the impedance spectra results reported in the previous work [32]. Although HVOF coatings are extremely compact/defect-free, they still have some pores (2–4% porosity) on the surface within the lamellae connecting boundaries and where the particles meet each other [33]; furthermore, surface pores can be seen in microstructure represented by R_{pore} . The CPE coat represents the capacitance at the coating. Inconel 625 consists of different oxidizing elements, i.e., Ni, Cr, Mo, Nb, etc., but Ni and Cr are considered as the primary oxide formers due to their higher percentage. Oxides and hydroxides of Ni and Cr may be present [34], but for simplicity, oxides are only considered as less stable and more stable. Oxides formed during the coating process around the splat boundaries

are more stable, while next to this region, there is a material that is depleted in Cr content and forms less stable oxides [6,35,36]. The freshly formed oxide on the surface is a layered structure, while the one formed during the coating process is embedded at different locations. The above situation suggests that oxides present in the coating cannot be modelled with stringent series or parallel circuitry, but still, the dominating factor can be considered while modelling. In the HVOF Inconel 625 coating, it is believed that layered oxide is dominant, and hence, the oxides are assumed to be in series. There are pores in the coating but not enough to

allow the electrolyte to pass through to the substrate; therefore, the coating capacitance is the dominating factor. Pores in the coatings allow a separate path for current flow; hence, they are in parallel with the oxide layer. The R_u is the solution resistance and is always in series with the rest of the circuit, while L represents the inductance involved in the coating. The induction effect is due to the current induced from the surrounding electrical equipment as well as of the instrument/cables itself. Additionally, it is proposed that the particles encapsulated into the oxide surrounding can also give induction behavior.

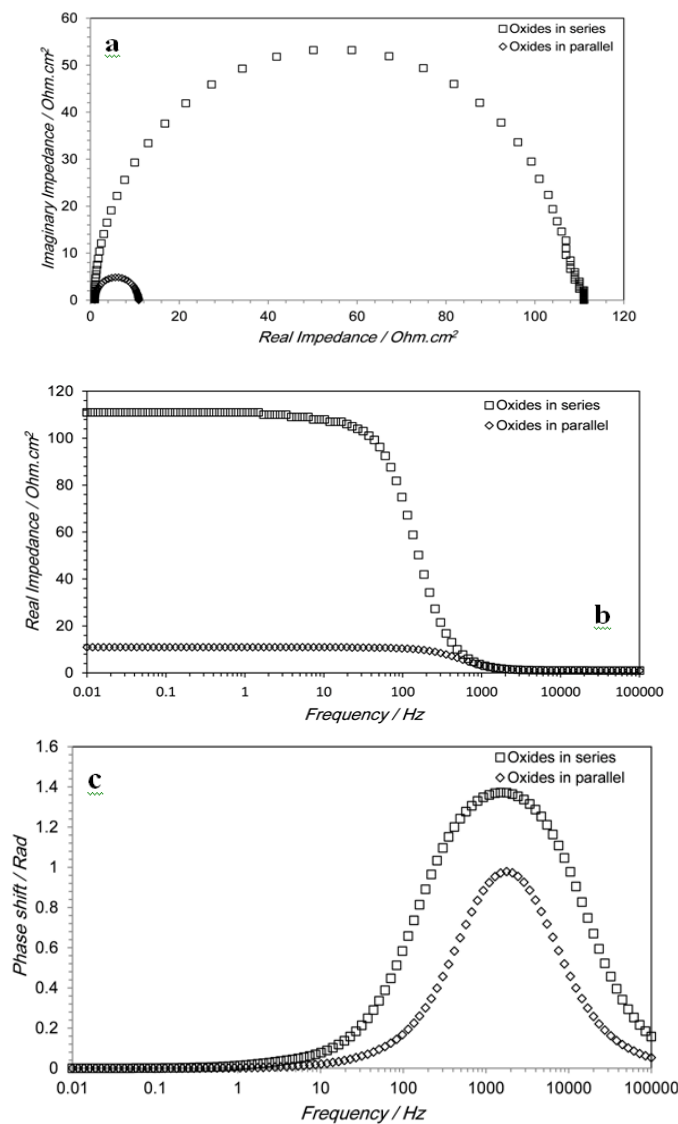


Fig. 11. EIS graphs; a) Nyquist plots, b) Bode impedance plots, c) Bode theta plots simulation is performed by using the equivalent circuit model in Fig. 10 for combined oxide and pores in parallel and series. The same circuit quantities are used for both circuits

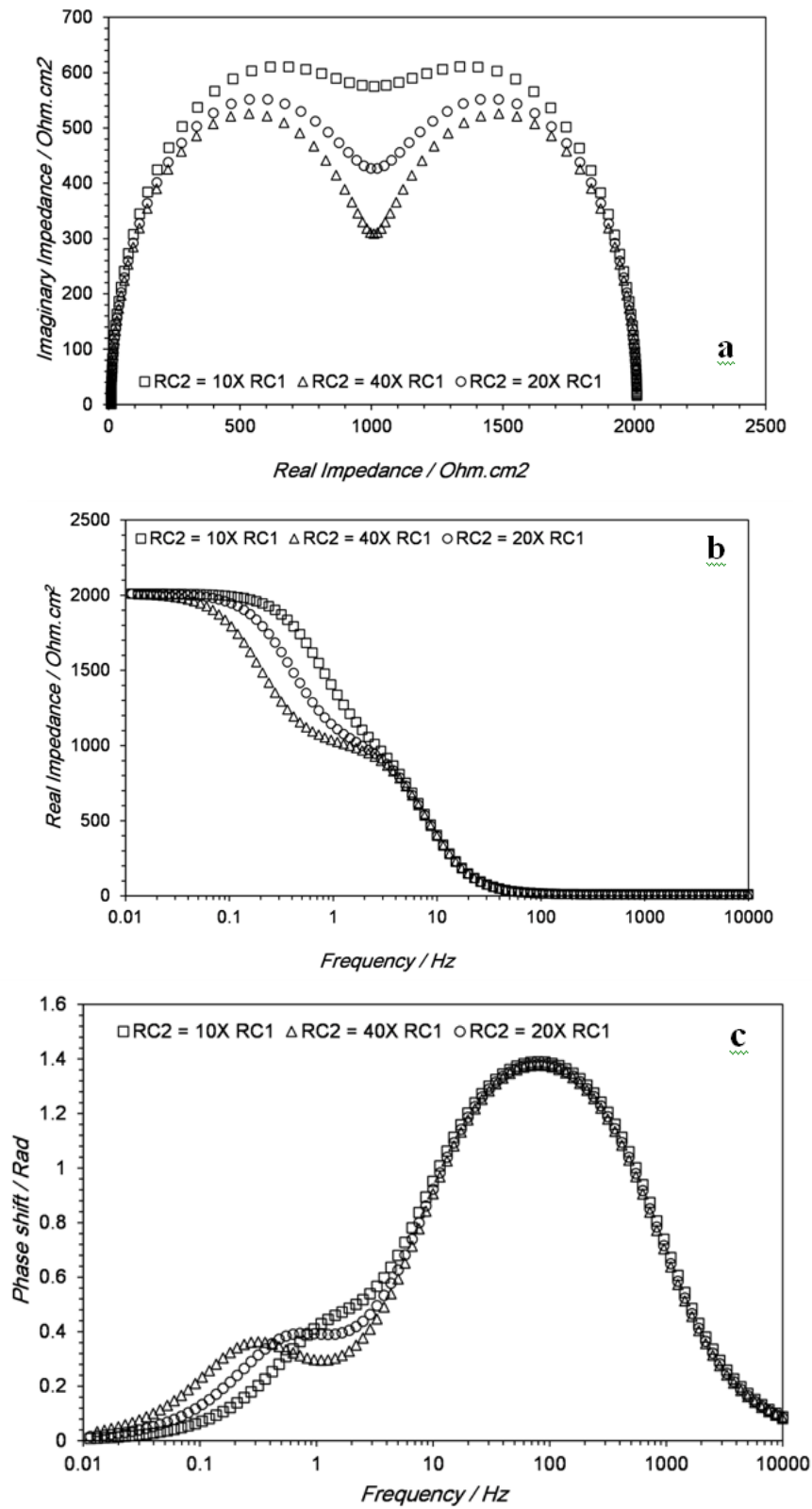


Fig. 12. EIS graphs; a) Nyquist plots, b) Bode impedance plots, c) Bode theta plots simulation is performed by using the equivalent circuit model in Fig. 9 for combined oxide and pores in parallel and series

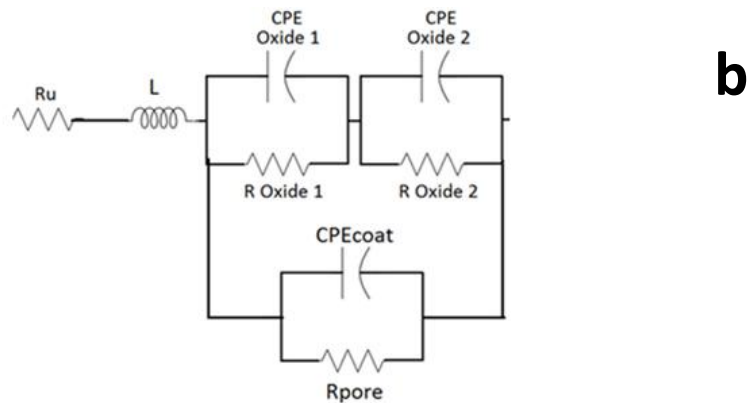
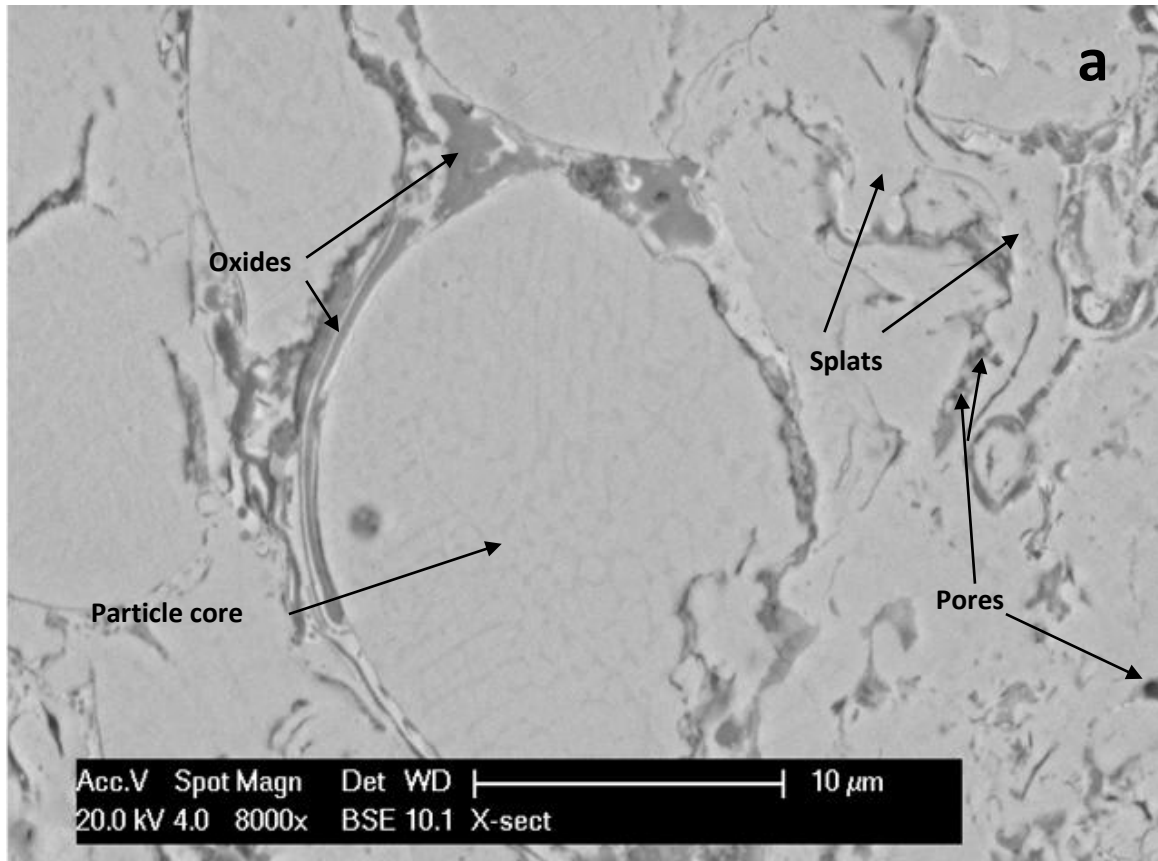


Fig. 13. a) Microstructure features of HVOF Inconel 625 coating, b) Proposed equivalent circuit model for HVOF coatings

3.3 Fitting the Equivalent Circuit Model to Real Coating

The EIS data recorded at Inconel-625 at the open circuit is fitted to the reported and the proposed equivalent circuit model in Fig. 14 to see the quality of fit. These results are not comparable with other reported ones, as different

components of the equivalent circuit are considered here.

The graphs in Fig. 14 and the results in Table 3 show that the quantities of most of the circuit components are within the error margin of 5 to 10% except for few that have higher error values. The experiment data is also fitted with the model

reported by different researchers to analyze the EIS results of HVOF metallic coatings, as shown in Fig. 14. The error margin is found to be lower with the reported model, but this analysis hides much useful information on the impedance

spectra. It may be advisable sometimes to use a simple ECM to express the corrosion process, but for a comprehensive approach, major corrosion processes must be considered.

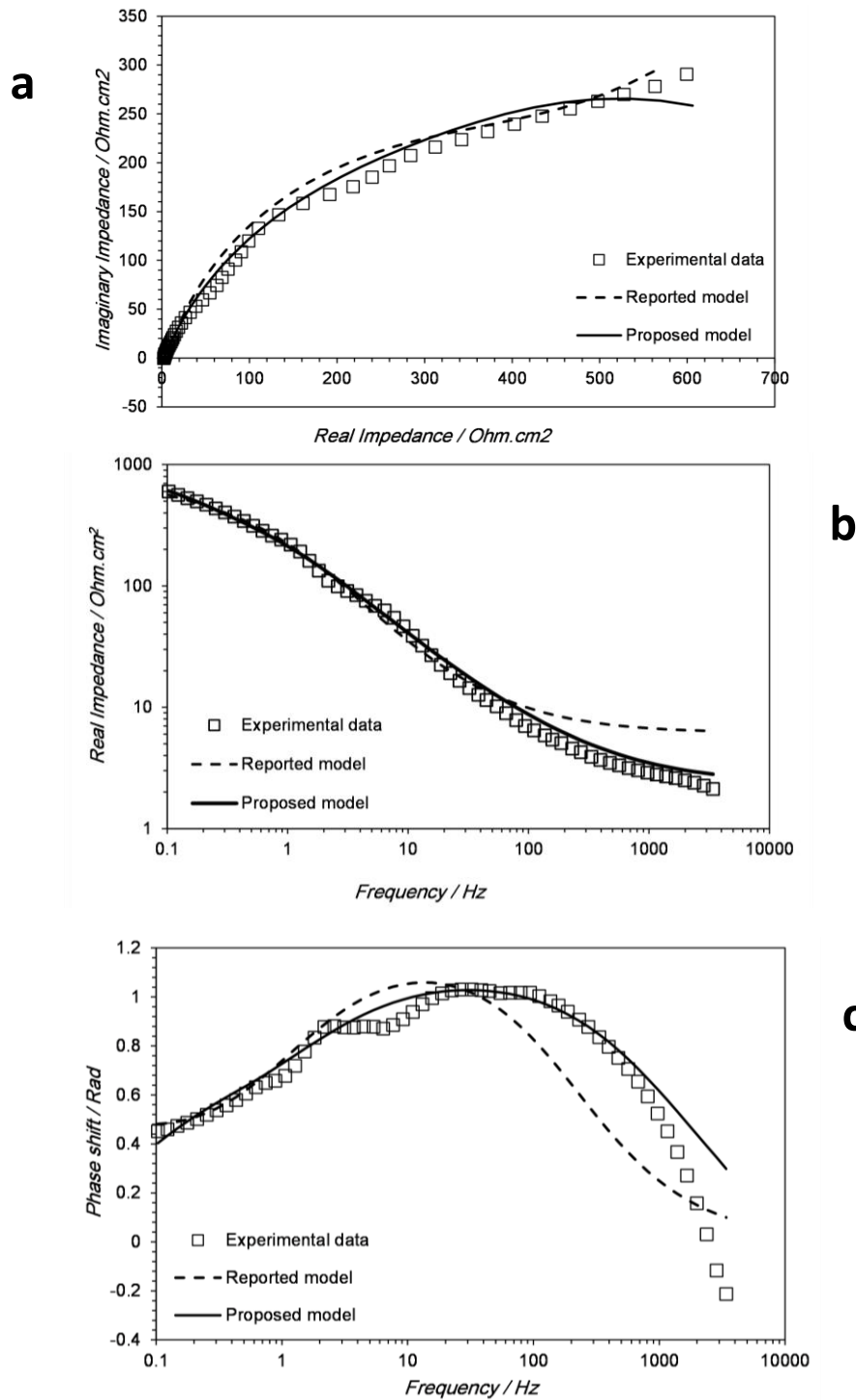


Fig. 14. Inconel 625 coatings EIS graphs fitted with the reported and proposed equivalent circuit models; a) Nyquist plots, b) Bode impedance plots, c) Bode theta plots
 Table 3. Seed values of the Inconel 625 coatings with reported model

Solution resistance R_u (Ω)	Warburg diffusion W_{diff} (Ω)	Constant phase element CPE		Polarization resistance R_p (Ω)	Model and experiment data
		P (μF)	n		
6.5	176	500	0.8	480	
63	6	5	2	3	Error %

Table 4. Seed values of the Inconel 625 coatings with proposed model

R_u (Ω)	R_{pore} (Ω)	R_{oxide1} (Ω)	R_{oxide2} (Ω)	CPE _{oxide1} (μF)		CPE _{oxide2} (μF)		CPE _{coat} (μF)		L ($\mu\Omega$)	Model and experiment data
				P ₁	n ₁	P ₂	n ₂	P ₃	n ₃		
3	966	521	85399	497	0.81	420	0.84	500	0.6	53	
--	3	29	--	12	5	31	11	7	4	--	Error %

In both model fittings (reported and proposed model), the simulated graph (solid line) does not overlap the all-experimental data points completely, probably due to the heterogeneous nature of the coating. This heterogeneity of the coatings does not allow stable electrochemical processes at the coating surface. The change is more pronounced in the Bode theta plot at lower frequencies (1–10 Hz). Though both models do not entirely fit with the experimental data, the visual appearance of the fitting of the proposed model is much improved as compared to the reported model.

The error values of some parameters of the proposed model are much higher than the reported model Table 4. It should be noted that the capacitance values used are realistic in comparison with the amounts reported in the literature (i.e., 10^{-5} – 10^{-7} $\mu F/cm^2$) [37-40]. The variation in the capacitance is due to the defective nature of the oxides on the HVOF coating. Additionally, an inductor is installed (proposed model) before the solution resistance to incorporate the inductance of the coatings. This is done to add the impedance contribution in the overall circuit due to the encapsulate oxides in the coatings.

4. SUMMARY

Through this exercise, we have tried to build up basic understandings of the complex corrosion processes taking place in multicomponent metallic coatings systems. The surface roughness, porosity, and multi-phase oxides are considered as major components of the coatings that contribute to the corrosion processes. These physical features are modelled into electrochemical equivalent circuits. The specific circuitry for each of the circuit-component is

configured by keeping in mind their presence in the coatings. The variation in the circuit components' quantities displays changes in the impedance spectra shape and overall impedance of the circuit. The nature of the element and its amounts contribute to the total impedance results. Furthermore, it is noted that by considering different physical processes in the corrosion system, we can make the equivalent circuit to be representative of the coatings with a little compromise on the quantitative results.

5. CONCLUSIONS

The stand-alone use of impedance spectroscopy technique to study complex microstructural features of HVOF metallic coatings revealed the following points.

The depressed shape of the semi-circle of the Nyquist plot is a characteristic property of impure capacitor. It is a well-established fact that the surface profiles of the HVOF coatings are mostly variant, where not only peak-to-valley distance change but also the geometry of peaks and valleys. The presence of phases with different levels of electrochemical activity, composition variation within the thickness of the coating, and local-current variation at the surface of the tested coating samples also exist. These all contribute to the overall change in the electrical double layer capacitance. The simulation results showed that the changing exponent of the CPE from 1 to 0.8 increases the depression of the Nyquist plot.

The surface porosity contributed to an increase of the coating capacitance and interconnected contributes to a decrease in the coating resistance. In this study, we consider that < 5 % porosity contributes to higher capacitance due to pore sealing, while > 5% porosity becomes interconnected and causes a decrease in the impedance. The contribution of 1-5% porosity

and 20-50% porosity is only overall change in the impedance values. The shape change in the Bode impedance plot is only visible from 5-20 % porosity.

In a multiphase oxide system, the phases of different conductivity, grain boundary accumulation system and the visible appearance in impedance spectra is only possible when the RC time constant of the processes are relatively diverse (>5% <100%). Furthermore, the processes have vastly close and vastly different RC, which generally gives cumulative impedance in the EIS results. Moreover, the change in the impedance spectra is more pronounced due to the capacitance increase (pore blocking/compact oxide) than the resistance increase (thickening oxide). The overall separation of the time constant lowers the impedance on the imaginary axis, but their cumulative impedance is always higher than the time constants summing each other (due to close RC).

The best fit with low error margins can be achieved with a simple equivalent circuit model, or with a trial and error method. However, proposing a logical equivalent circuit and acquiring a best fit is somewhat more daunting task in the coatings like Inconel-625 where microstructural features are not widely different from each other as compared to cermet and thermal barrier coatings. Therefore, elucidating microstructural features, proposing an equivalent circuit model is an add-on to the knowledge of the coatings, but still achieving a good fit between the practical and proposed model is needs to be explored in the future.

DISCLAIMER

The products used for this research are commonly and predominantly use products in our area of research and country. There is absolutely no conflict of interest between the authors and producers of the products because we do not intend to use these products as an avenue for any litigation but for the advancement of knowledge. Also, the research was not funded by the producing company rather it was funded by personal efforts of the authors.

COMPETING INTERESTS

Authors have declared that no competing interests exist.

REFERENCES

1. Neville A, Perry JM, Hodgkiess T, Chua HP. Wrought and high-velocity oxy fuel

sprayed Inconel 625 examination of corrosion aspects. *P. Mech. Eng. L. J. Mat.* 2000;214(1):41-48.

DOI: 10.1177/146442070021400106

2. Verdian MM, Raeissi K, Salehi M. Corrosion performance of HVOF and APS thermally sprayed NiTi intermetallic coatings in 3.5% NaCl solution. *Corros. Sci.* 2009;52(3):1052-1059. Available: <https://doi.org/10.1016/j.corosci.2009.11.034>
3. Pougoum F, Qian J, Martinu L, Klemberg-Sapieha J, Zhou Z, Li KY, Savoie S, Lacasse R, Potvin E, Schulz R. Study of corrosion and tribocorrosion of Fe3Al-based duplex PVD/HVOF coatings against alumina in NaCl solution. *Surf. Coat. Technol.*, 2018;357:774-783. Available: <https://doi.org/10.1016/j.surfcoat.2018.10.060>
4. Duan Z, Yang H, Kano S, Murakami K, Satoh Y, Takeda Y, Abe H. Oxidation and electrochemical behaviors of Al₂O₃ and ZrO₂ coatings on Zircaloy-2 cladding by thermal spraying. *Surf. Coat. Technol.* 2017;334:319-327. Available: <https://doi.org/10.1016/j.surfcoat.2017.11.050>
5. Guo RQ, Zhang C, Chen Q, Yang Y, Li N, Liu L. Study of structure and corrosion resistance of Fe-based amorphous coatings prepared by HVOF and HVOF. *Corros. Sci.* 2010;53(7):2351-2356. Available: <https://doi.org/10.1016/j.corosci.2010.12.022>
6. Verdian MM, Raeissi K, Salehi M, Electrochemical impedance spectroscopy of HVOF-sprayed NiTi intermetallic coatings deposited on AISI 1045 steel. *J. Alloys. Compd.*, 2010;507(1):42-46. Available: <https://doi.org/10.1016/j.jallcom.2010.07.132>
7. Ahmed R, Vourlias G, Algoburi A, Vogiatzis C, Chaliampalias D, Skolianos S, Berger LM, Paul S, Faisal NH, Toma FL, Al-Anazi NM, Goosen MFA. Comparative Study of Corrosion Performance of HVOF-Sprayed Coatings Produced Using Conventional and Suspension WC-Co Feedstock. *J. Therm. Spray Technol.* 2018;27(8):1579-1593. DOI: 10.1007/s11666-018-0775-2
8. Sadeghi E, Markocsan N, Nylen P. A Comparative Study of Corrosion Resistance for HVOF-Sprayed Fe- and Co-Based Coatings. *J. Coat. Technol. Res.* 2016;6:1.

- DOI: 10.3390/coatings6020016
9. Hong S, Wu Y, Zheng Y, Wang B, Gao W, Li G, Ying G, Lin J. Effect of Spray Parameters on the Corrosion Behavior of HVOF Sprayed WC-Co-Cr Coatings. *J. Mater. Eng. Perform.* 2014;23(4):1434-1439.
DOI: 10.1007/s11665-014-0865-3
 10. Melero HC, Sakai RT, Vignatti CA, Benedetti AV, Fernandez J, Guilemany JM, Suegama PH. Corrosion Resistance Evaluation of HVOF Produced Hydroxyapatite and TiO₂-hydroxyapatite Coatings in Hanks' Solution. *Mater. Res.* 2018;21.
DOI: 10.1016/j.electacta.2003.09.017
 11. Suegama P, Fugivara C, Benedetti, A, Guilemany JM, Fernandez J, Delgado J. The influence of gun transverse speed on electrochemical behaviour of thermally sprayed Cr₃C₂ NiCr coatings in 0.5 M H₂SO₄ solution. *Electrochim. Acta.* 2004;49:627-634.
DOI: 10.1016/s0257-8972(01)01679-6
 12. Guilemany JM, Fernandez J, Delgado J, Benedetti A, Climent F. Effects of thickness coating on the electrochemical behaviour of thermal spray Cr₃C₂ NiCr coatings. *Surf. Coat. Technol.* 2002;153: 107-113.
DOI: 10.1016/s0257-8972(01)01679-6
 13. Ali MS, Song S, Xiao P. Evaluation of degradation of thermal barrier coatings using impedance spectroscopy. *J. Eur. Ceram. Soc.* 2002;22(1):101-107.
Available: [https://doi.org/10.1016/S0955-2219\(01\)00234-5](https://doi.org/10.1016/S0955-2219(01)00234-5)
 14. Antou G, Montavon G, Hlawka F, Cornet A, Coddet C. Exploring thermal spray gray alumina coating pore network architecture by combining stereological protocols and impedance electrochemical spectroscopy. *J. Therm. Spray Technol.* 2006;15(4): 765-772.
DOI: 10.1361/105996306x147045
 15. Amsellem O, Borit F, Jeulin D, Guipont V, Jeandin M, Boller E, Pauchet F. Three-Dimensional Simulation of Porosity in Plasma-Sprayed Alumina Using Microtomography and Electrochemical Impedance Spectrometry for Finite Element Modeling of Properties. *J. Therm. Spray Technol.* 2012;21(2):193-201.
DOI: 10.1007/s11666-011-9687-0
 16. Zhang S-L, Huang J-Y, C-X. Li, Yang G-J, Li C-J. Relationship Between Designed Three-Dimensional YSZ Electrolyte Surface Area and Performance of Solution-Precursor Plasma-Sprayed La_{0.8}Sr_{0.2}MnO_{3-δ} Cathodes. *J. Therm. Spray Technol.* 2016;25(8):1692-1699.
DOI: 10.1007/s11666-016-0466-9
 17. Bolelli G, Meschini D, Varis T, Testa V, Morelli S, Lusvarghi L, Vuoristo P. Corrosion Properties of Thermally Sprayed Bond Coatings Under Plasma-Sprayed Chromia Coating in Sulfuric Acid Solutions. *J. Therm. Spray Technol.* 2019.
DOI: 10.1007/s11666-019-00922-9
 18. Chen W-L, Liu M, Zhang J-F. Impedance Analysis of 7YSZ Thermal Barrier Coatings During High-Temperature Oxidation. *J. Therm. Spray Technol.*, 2016;25(8):1596-1603.
DOI: 10.1007/s11666-016-0471-z
 19. Cheng JB, Liang XB, Xu BS. Effects of Crystallization on the Corrosion Resistance of Arc-Sprayed FeBSiNb Coatings. *J. Therm. Spray Technol.* 2014;23(3):373-379.
DOI: 10.1007/s11666-013-9990-z
 20. Cojocar CV, Lamarre JM, Legoux JG, Marple BR. Atmospheric Plasma Sprayed Forsterite (Mg₂SiO₄) Coatings: An Investigation of the Processing-Microstructure-Performance Relationship. *J. Therm. Spray Technol.* 2013;22(2):145-151.
DOI: 10.1007/s11666-012-9856-9
 21. Chenchen G, Liyong N, Zhou C. Evaluation of Microstructural Evolution of Nanostructured Yttria-stabilized Zirconia During Sintering Using Impedance Spectroscopy. *J. Therm. Spray Technol.* 2012;21(5):1076-1082.
DOI: 10.1007/s11666-012-9787-5
 22. RGA Bondarenko AS. *Progress in Chemometrics Research*, Pomerantsev A. L. Ed. Nova Science Publishers: New York. 2005;89-102.
 23. Huang J, Li Z, Liaw BY, Zhang J. Graphical analysis of electrochemical impedance spectroscopy data in Bode and Nyquist representations. *J. Power Sources.* 309:82-98.
Available: <https://doi.org/10.1016/j.jpowsour.2016.01.073>
 24. Boukamp BA. Practical application of the Kramers-Kronig transformation on impedance measurements in solid state electrochemistry. *Solid State Ion.* 1993; 62(1):131-141.
Available: [https://doi.org/10.1016/0167-2738\(93\)90261-Z](https://doi.org/10.1016/0167-2738(93)90261-Z)

25. Qiao L, Wu Y, Hong S, Cheng J, Wei Z. Influence of the high-velocity oxygen-fuel spray parameters on the porosity and corrosion resistance of iron-based amorphous coatings. *Surf. Coat. Technol.* 2019;366:296-302.
Available:<https://doi.org/10.1016/j.surfcoat.2019.03.046>
26. D'souza MEP, Ariza E, Ballester M, Yoshida IVRP, Rocha LA, Freire CLMDA. Characterization of organic-inorganic hybrid coatings for corrosion protection of galvanized steel and electroplated ZnFe steel. *Mater. Res.* 2006;9:59-64.
27. Yao H-L, Zou Y-L, Bai X-B, Wang H-T, Ji G-C, Chen Q-Y. Microstructures, mechanical properties and electrochemical behaviors of nano-structured HA/Ti composite coatings deposited by high-velocity suspension flame spray (HVSFS). *Ceram. Int.*, 2018;44(11):13024-13030.
Available:<https://doi.org/10.1016/j.ceramint.2018.04.121>
28. Gomez-Vidal JC, Fernandez AG, Tirawat R, Turchi C, Huddleston W. Corrosion resistance of alumina-forming alloys against molten chlorides for energy production. I: Pre-oxidation treatment and isothermal corrosion tests. *Sol. Energy Mater. Sol. Cells.* 2017;166:222-233.
Available:<https://doi.org/10.1016/j.solmat.2017.02.019>
29. Suresh Babu P, Chanikya Rao P, Jyothirmayi A, Sudharshan Phani P, Rama Krishna L, and Srinivasa Rao D. Evaluation of microstructure, property and performance of detonation sprayed WC-(W,Cr)2C-Ni coatings. *Surf. Coat. Technol.* 2017;335:345-354.
Available:<https://doi.org/10.1016/j.surfcoat.2017.12.055>
30. Verdian MM, Raeissi K, Salehi M. Corrosion resistance of HVOF-sprayed Ni2Si intermetallic coatings in hot H2SO4 medium. *Surf. Coat. Technol.* 2013; 240:70-75.
DOI: 10.1016/j.surfcoat.2013.12.016
31. Niaz A, Bakare M. Electrochemical corrosion testing and characterization of potential assisted passive layer on HVOF Inconel 625 coating. *Corros. Rev.* 2014;33.
DOI: 10.1515/correv-2014-0037
32. Niaz A, Khan SU. A Comprehensive Pitting Study of High Velocity Oxygen Fuel Inconel 625 Coating by Using Electrochemical Testing Techniques. *J. Mater. Eng. Perform.* 2016;25(1):280-289.
DOI: 10.1007/s11665-015-1846-x
33. Ahmed N, Bakare MS, Mc Cartney DG, Voisey KT. The effects of microstructural features on the performance gap in corrosion resistance between bulk and HVOF sprayed Inconel 625. *Surf. Coat. Technol.* 2009;204(14):2294-2301.
Available:<https://doi.org/10.1016/j.surfcoat.2009.12.028>
34. Bakare MS, Voisey KT, Roe MJ, McCartney DG. X-ray photoelectron spectroscopy study of the passive films formed on thermally sprayed and wrought Inconel 625. *App. Surf. Sci.* 2010;257(3): 786-794.
Available:<https://doi.org/10.1016/j.apsusc.2010.07.066>
35. Lim YS, Kim HP, Kim JS, Kwon HS. Double loop electrochemical potentiokinetic reactivation test of Nickel-base Alloy 600 surface-melted by a CO2 laser beam. *Met. Mater. Int.* 2001;7(1):61-65.
DOI: 10.1007/bf03026940
36. Wu T-F, Tsai W-T. Effect of KSCN and its concentration on the reactivation behavior of sensitized alloy 600 in sulfuric acid solution. *Corros. Sci.* 2003;45(2):267-280.
Available:[https://doi.org/10.1016/S0010-938X\(02\)00100-2](https://doi.org/10.1016/S0010-938X(02)00100-2)
37. Da M, Cunha Belo, Hakiki NE, Ferreira MGS. Semiconducting properties of passive films formed on nickel and base alloys type Alloy 600: influence of the alloying elements. *Electrochim. Acta.* 1999; 44(14):2473-2481.
Available:[https://doi.org/10.1016/S0013-4686\(98\)00372-7](https://doi.org/10.1016/S0013-4686(98)00372-7)
38. Lloyd AC, Noel JJ, Shoesmith D, McIntyre N. The open-circuit ennoblement of alloy C-22 and other Ni-Cr-Mo alloys. *J. Minerals, Metals & Materials Society.* 2005;57:31-35.
DOI: 10.1007/s11837-005-0061-x
39. Zhang Y, Feng H, Wu X, Wang L, Zhang A, Xia T, Dong H, Li X, Zhang L. Progress of Electrochemical Capacitor Electrode Materials: A Review. *Int. J. Hydrogen. Energy.* 2009;34:4889-4899.
DOI: 10.1016/j.ijhydene.2009.04.005

40. Bai H, Wang F. Protective Properties of High Temperature Oxide Films on Ni-based Superalloys in 3.5% NaCl Solution. J. Mater. Sci. Technol. 2007;23.

© 2021 Niaz et al.; This is an Open Access article distributed under the terms of the Creative Commons Attribution License (<http://creativecommons.org/licenses/by/4.0>), which permits unrestricted use, distribution, and reproduction in any medium, provided the original work is properly cited.

Peer-review history:

The peer review history for this paper can be accessed here:
<http://www.sdiarticle4.com/review-history/69155>